Acta Materialia 298 (2025) 121366

Contents lists available at ScienceDirect

Acta Materialia

journal homepage: www.elsevier.com/locate/actamat

Full length article

Kinked basal dislocation loops for anomalous annealing hardening in irradiated zirconium

Si-Mian Liu [a,1], Shi-Hao Zhang [b,1], Hiroaki Abe [c], Shigenobu Ogata [b,*], Wei-Zhong Han [a,*]

[a] Center for Advancing Materials Performance from the Nanoscale, State Key Laboratory for Mechanical Behavior of Materials, Xi'an Jiaotong University, Xi'an 710049, China
[b] Department of Mechanical Science and Bioengineering, The University of Osaka, Osaka 560-8531, Japan
[c] Nuclear Professional School, The University of Tokyo, Tokai, Ibaraki 319-1188, Japan

ARTICLE INFO

Keywords:
Zirconium
Irradiation
Annealing
Hardening
Dislocation loop

ABSTRACT

Annealing is a traditional pathway to mitigate irradiation hardening in metals, while an anomalous annealing hardening is widely observed in neutron-irradiated zirconium (Zr), which is counterintuitive and intriguing, and affects the performance of Zr components in nuclear reactors. Here, we report that the anomalous annealing hardening in irradiated Zr originates from thermally activated formation of three-dimensional kinked ⟨c⟩ dislocation loops. Through concurrent in-situ heating experiments inside a transmission electron microscope, we demonstrate that irradiation-induced planar ⟨c⟩ dislocation loops progressively merge into zigzag-shape kinked configurations between 400 °C -500 °C. Atomistic simulations reveal that partial dislocations generated by the dissociation of 1/6 $<2\bar{2}03>$ loops glide on pyramidal planes driven by the inter-loop attraction forces, ultimately forming kinked steps. These three-dimensional kinked ⟨c⟩ loops act as strong obstacles for prismatic ⟨a⟩ dislocations, leading to a pronounced hardening. This discovery provides a universal framework for understanding the annealing-induced hardening in hexagonal close-packed metals.

1. Introduction

Structural materials for nuclear applications face persistent degradation due to prolonged exposure to high-energy particle bombardment, which generates a high density of vacancies and interstitials. At elevated temperatures, the migration and aggregation of these point defects lead to the formation of extended defects, including dislocation loops, stacking fault tetrahedra (SFTs), vacancy platelets, voids, and gas bubbles [1–6]. These defects interact with dislocations, driving critical property changes in nuclear reactor components—such as irradiation hardening [7–9], strain localization [10,11], and irradiation-induced dimensional instabilities (e.g. irradiation growth and creep) [12–14]. While irradiation hardening exacerbates material embrittlement, post-irradiation annealing can partially mitigate this by defect annihilation [15]. Intriguingly, neutron-irradiated hexagonal close-packed (HCP) metals like zirconium (Zr) alloys exhibit an anomalous hardness increase upon annealing [16–20], a phenomenon that defies conventional understanding and demands mechanistic elucidation. The annealing occurs during the dry-out stage of Zr alloy cladding tubes after service in nuclear reactors [20]. The resulting temperature rise can alter the mechanical properties of tubes that were already hardened by irradiation defects, and crucially, the anomalous annealing hardening poses challenges for the subsequent long-term storage of spent nuclear fuel. Therefore, understanding the underlying mechanisms of anomalous annealing-hardening in Zr alloys is not only academically intriguing but also important for predicting component behavior during reactor transients and ensuring the safe, long-term storage of nuclear waste.

Zr alloys develop irradiation-induced ⟨a⟩ and ⟨c⟩ dislocation loops. ⟨a⟩ loops (interstitial/vacancy type), with Burgers vectors of 1/3 $<11\bar{2}0>$ on the prismatic plane undergo coarsening and annihilation at higher temperatures, marginally reducing yield strength and hardness of Zircaloy [21,22]. In contrast, faulted ⟨c⟩ loops (vacancy type), with Burgers vector of 1/6 $<20\bar{2}3>$ on the basal plane remain thermal stable at service temperatures (300 °C-400 °C) [23–26]. Strikingly, annealing above 400 °C triggers pronounced hardening in irradiated Zr alloys [17–20]. Since ⟨a⟩ loops are conventionally linked to irradiation hardening [7,8], three hypotheses have been proposed for this anomaly: (1) Growth of nano-sized ⟨a⟩ loops or voids during the short annealing stage

* Corresponding authors.
E-mail addresses: ogata@me.es.osaka-u.ac.jp (S. Ogata), wzhanxjtu@mail.xjtu.edu.cn (W.-Z. Han).
[1] These authors contributed equally to this work.

https://doi.org/10.1016/j.actamat.2025.121366
Received 31 March 2025; Received in revised form 29 June 2025; Accepted 19 July 2025
Available online 20 July 2025

above 400 °C [27,28]; (2) Segregation of Fe, Sn, and Cr solutes at ⟨a⟩ loops [28]; and (3) Impurity-defect interactions (e.g., oxygen/hydrogen with ⟨a⟩ loops) [19]. However, these mechanisms remain elusive owing to the difficulty in identifying the detailed characteristics of irradiation defects and clarifying the role of alloying elements in post-radiation annealing hardening.

In this contribution, we isolate the intrinsic defect dynamics in Zr by employing high-purity samples, eliminating confounding effects from alloy elements, and unveil the critical role of kinked ⟨c⟩ dislocation loops in annealing hardening. In-situ high-temperature nanoindentation reveals significant annealing hardening above 400 °C. Complementary in-situ transmission electron microscopy (TEM) annealing experiments uncover a structural transition: two-dimensional flat ⟨c⟩ loops evolve into three-dimensional kinked configurations between 400 °C-500 °C. Atomistic simulations further validated that these kinked ⟨c⟩ loops impose potent barriers to ⟨a⟩ dislocation glide, directly linking defect morphology evolution to the anomalous hardening.

2. Methods

2.1. Sample preparation

High-purity Zr (99.9 %) was used in this study. Detailed information on the material composition can be found in Table S1 in the Supplementary Materials. The high-purity Zr sample was annealed prior to irradiation to eliminate existing defects. The annealing process was conducted in a high vacuum tube furnace with a vacuum better than 10^{-5} Pa for 3 h. The annealed sample exhibited an average grain size of approximately 100 μm. The sample was then punched into TEM thin foil with a diameter of 3 mm and subsequently electropolished using a solution of 90 % methanol and 10 % perchloric acid at −30 °C. To exclude the potential impact of different irradiated ions on the formation of kinked ⟨c⟩ loops, both Kr and Fe ions were employed for irradiation experiments. Kr^{2+} ions (800 keV) irradiation was performed at 400 °C to a fluence of 5×10^{15} ions m^{-2} with a flux rate of 4.6×10^{12} ions $m^{-2}s^{-1}$ in the NEC 400 kV Implanter. Fe^{2+} ions (2.8 MeV) irradiation was conducted at about 307 °C with a fluence rate of 1.76×10^{12} ions $m^{-2}s^{-1}$ in the High Fluence Irradiation Facility (HIT) at the University of Tokyo [29]. The irradiation damage and implanted ions concentration were calculated using SRIM with full damage cascades mode with displacement energy of 40 eV for Zr [30,31]. Fig. 1 shows that the damage is about 33 dpa for Kr^{2+} irradiation and 5 dpa for Fe^{2+} irradiation at the depth of 200 nm. Radiation defects were characterized using a conventional TEM diffraction contrast technique inside a JEOL 2100F. Notably, no voids nor bubbles were observed in samples irradiated with either Kr^{2+} or Fe^{2+} ions.

2.2. High-temperature nanoindentation test

Quantitative nanoindentation tests were performed on post-irradiated bulk Zr using an FT-NMT04 In-Situ Nanoindenter integrated within a dual beam SEM/FIB (ZEISS Crossbeam 550). A Kr^{2+} irradiated Zr sample with a thickness of 0.2 mm was mounted on the heating sample holder using screw fasteners, as shown in Fig. 2(a). The equipped diamond Berkovich tip was calibrated using a standard fused quartz. Nanoindentation experiments were carried out in continuous stiffness measurement (CSM) to analyze the hardness change in the damaged area of the material. Tests were performed to a maximum depth of 500 nm and a constant loading rate of 100 nm/s at 25 °C, 400 °C, and 500 °C. The temperature stabilization period required 30–35 min for heating and 180–200 min for cooling. Hardness values corresponding to an indentation depth of 200 nm were analyzed, representing the peak damage region as determined by SRIM calculation (Fig. 1). For each temperature condition, average hardness values were determined from a minimum of 20 replicate tests, with adjacent indentation sites spaced approximately 5 μm apart, as shown in the insert in Fig. 2(a). All indentations were performed within a single grain exhibiting the orientation of $[\bar{3}\bar{3}6\bar{1}]$ (see Fig. S1), which was determined by Electron Backscattered Diffraction (EBSD). Load-displacement curves were systematically analyzed, and the hardness values were calculated via the load/contact area relationship.

2.3. In-situ annealing inside a TEM

In-situ annealing was carried out using a double-tilt Gatan heating holder in a JEOL-2000EX TEM operated at 200 kV. The maximum annealing temperature is 498 °C with a heating rate of 1.5∼1.7 °C/min. Samples were sequentially maintained at 300 °C, 400 °C, and 498 °C for 1 h each to systematically characterize dislocation loop evolution. Post-annealing microstructural analysis was conducted using a JEOL-2100F TEM equipped with two-beam bright-field (BF) and weak-beam dark-field (WBDF) imaging modes. The Burgers vectors of ⟨c⟩ loops were determined through the $\vec{g}\cdot\vec{b}=0$ invisibility criterion. After annealing, samples were cooled to room temperature at a controlled rate of 4 °C/min. Real-time microstructural evolution during thermal processing was documented via a charge-coupled device (CCD) camera, capturing both high-resolution TEM images and time-lapse videos.

2.4. Atomistic simulations

Atomistic simulations were performed using the Large-scale Atomic/Molecular Massively Parallel Simulator (LAMMPS) code [32]. The embedded atom method (EAM) potential for Zr developed by Mendelev and Ackland [33] was employed, which has been extensively validated for studying the vacancy and interstitial dislocation loops in pure Zr

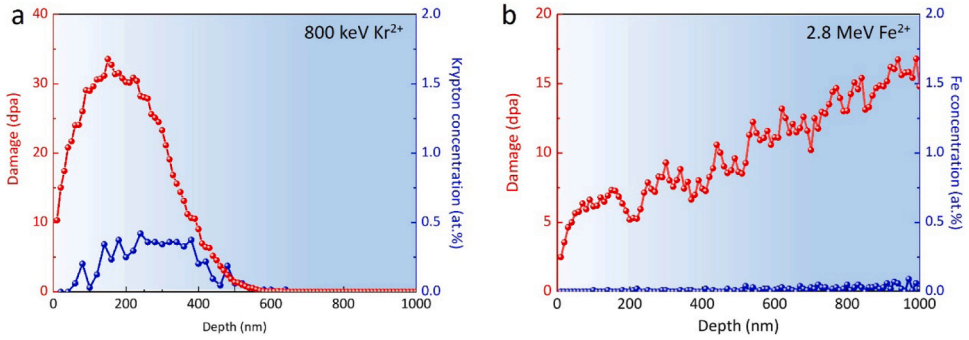

Fig. 1. Variation of radiation damage and concentration of implanted ions with irradiation depth. (a) krypton ion irradiated Zr (b) iron ion irradiated Zr. The SRIM calculation was conducted with a total number of 9999 krypton and iron ions with a full damage cascade method. The red curves are the radiation damage distribution and the blue ones show the implanted ion concentration.

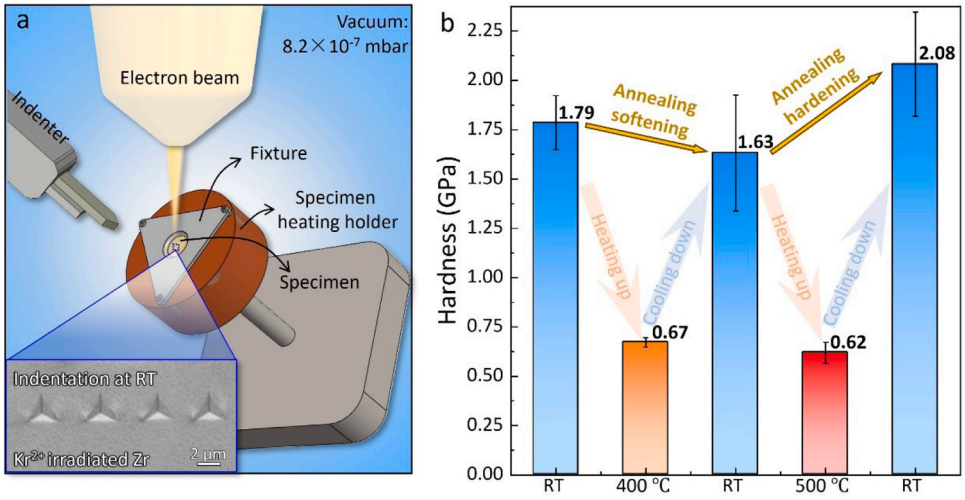

Fig. 2. Hardness of Zr after irradiation and annealing. (a) Schematic diagram of the hardness test method using in-situ nanoindentation in a high-vacuum chamber. Insert in the lower left corner is the SEM image of the irradiated pure Zr after nanoindentation. (b) Hardness of pure Zr after krypton irradiation, before and after annealing at 400 °C and 500 °C for 30 mins.

[34–37]. A simulation cell with dimensions of 3.2 nm (X), 10 nm (Y), and 40 nm (Z) was constructed, containing a straight dislocation with Burgers vector of 1/6 <2$\bar{2}$03>. Initial energy minimization was performed to optimize the dislocation configuration. The critical resolved shear stress (CRSS) for partial 1/6[$\bar{1}$102] dislocation slip on the {10$\bar{1}$1} plane was determined using nudged elastic band (NEB) analysis [38]. To investigate the dislocation-dissociation-mediated formation of three-dimensional ⟨c⟩ loop, simulations were performed in the NVT ensemble at 1200 K. This elevated temperature, significantly higher than the experimental condition of 500 °C (773 K), was selected to overcome the inherent timescale limitations of atomic simulations while accelerating the physical processes of ⟨c⟩ loop formation. The atomic configurations of the dislocation loops were analyzed and visualized with the common neighbor analysis (CNA) [39] and the dislocation extraction algorithm (DXA) [40] implemented in the OVITO program [41].

3. Results

3.1. Annealing hardening in irradiated Zr

Fig. 2b illustrates the temperature-dependent nanoindentation hardness of pure Zr. At RT, irradiated Zr exhibits a hardness of 1.78 ± 0.14 GPa. A distinct softening was observed when annealing at 400 °C. Upon cooling from 400 °C to RT, the hardness decreased to 1.63 ± 0.29 GPa, which is related to the recovery of those easy glide irradiation

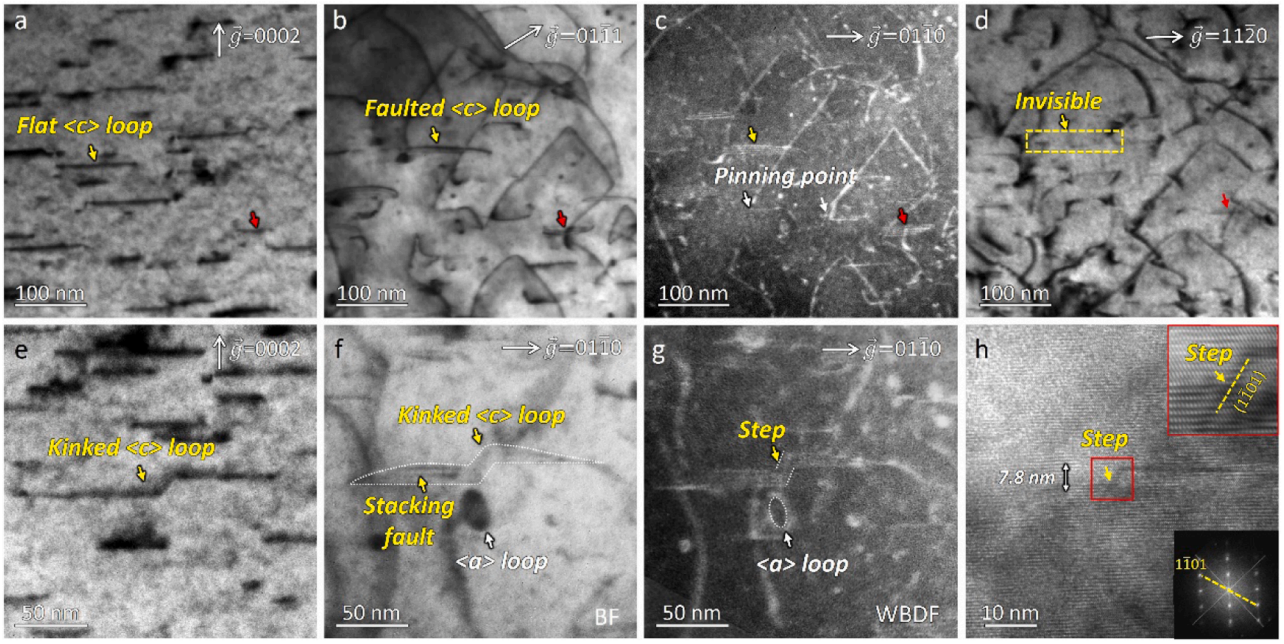

Fig. 3. Detailed characterization of flat and kinked ⟨c⟩ loops. (a-d) TEM images of the faulted flat ⟨c⟩ loops in the same region with different diffraction vectors (a) $\vec{g}$=0002; (b) $\vec{g}$=01$\bar{1}$1; (c) $\vec{g}$=01$\bar{1}$0; and (d) $\vec{g}$=11$\bar{2}$0. The red and yellow arrows mark the same variant of dislocation loops under different diffraction vectors, respectively. (e) TEM image of the kinked and faulted ⟨c⟩ loop viewed with diffraction vector of $\vec{g}$=0002. (f) Bright-field TEM image showing the same ⟨c⟩ loop under $\vec{g}$=01$\bar{1}$0 diffraction vector. (g) Weak-beam dark-field TEM image showing the same region in (f). (h) High-resolution TEM image showing the step height of the kinked ⟨c⟩ loop. The insert in the lower right corner is the inverse Fourier transformation image of the region.

defects, such as ⟨a⟩ loops. Remarkably, after annealing at 500 °C for 30 mins and cooling back to RT, the hardness of the sample increases to 2.08 GPa—a 25 % enhancement (0.45 GPa) compared to the 400 °C case, as shown in Fig. 2b This anomalous hardening aligns with neutron-irradiated Zircaloy alloys [18–20], suggesting a universal phenomenon in HCP metals.

3.2. Formation of kinked ⟨c⟩ dislocation loop

Irradiation of high-purity Zr with 800 keV Kr^{2+} ions produced abundant planar ⟨c⟩ dislocation loops observed under $\vec{g}$=0002, as shown in Fig. S2a. After annealing at 500 °C for 1 h in high vacuum environment, lots of kinked ⟨c⟩ loops appear (Fig. S2b). Fig. 3 shows a detailed characterization of the ⟨c⟩ loops in irradiated Zr before and after annealing, utilizing two-beam bright-field TEM imaging and weak-beam dark-field (WBDF) TEM imaging under specific diffracting vectors. Pre-annealed ⟨c⟩ loops displayed planar configuration under the viewing direction of $[1\bar{1}00]$ and $[\bar{2}110]$ zone axes. Their alignment perpendicular to the $\vec{g}$=0002 diffraction vector, indicating that they are lying on the basal plane (Fig. 3a). The clear fault fringes inside loops with $\vec{g}=01\bar{1}1$ (Fig. 3b) and $\vec{g}=01\bar{1}0$ (Fig. 3c) confirm the Burgers vector as 1/6 <20$\bar{2}$3>, distinct from 1/2[0001] [23]. The loop indicated by the yellow arrow lost contrast under $\vec{g}=11\bar{2}0$ (Fig. 3d), suggesting that this ⟨c⟩ loop has a Burgers vector of $1/6[2\bar{2}03]$ or $1/6[2\bar{2}0\bar{3}]$. Notably, following annealing at 500 °C, ⟨c⟩ loops transformed into interconnected linear segments with inclined steps under the $\vec{g}$=0002, as shown in Fig. 3e. WBDF imaging shown in Fig. 3g revealed that the inclined step between the two faulted loops has a measurable width, suggesting that the ⟨c⟩ loop now has a three-dimensional configuration, which is named kinked ⟨c⟩ loop hereafter. High-resolution TEM images reveal that this step corresponds to the pyramidal plane $\{1\bar{1}01\}$ (Fig. 3h). The height of the steps varies from 5 nm to 20 nm, with an interacting angle in the range of 30° to 60°, as shown by statistics in Fig. 4a. The kinked ⟨c⟩ loops have a morphology akin to the step-shaped ⟨$c+a$⟩ dislocations in HCP metals [42,43], which were also observed in the experiment but with low number density (Fig. S3).

3.3. Evolution of irradiation defects during in-situ annealing

To investigate the dynamic evolution processes of the three-dimensional ⟨c⟩ loops, we conducted in-situ TEM annealing experiments on 2.8 MeV Fe^{2+} ions irradiated high-purity Zr. Post-irradiation analysis revealed a high density of both ⟨a⟩ and ⟨c⟩ dislocation loops, as shown in Fig. 5a and b, with respect average diameters of 3.2 ± 0.8 nm and 61 ± 31.6 nm (see Fig. 4b). The size of flat ⟨c⟩ loops is smaller than that after Kr^{2+} irradiation (100 ± 25 nm) because of their difference in irradiation damage (5 dpa versus 33 dpa). A stepwise isothermal annealing process (300 °C/1 h → 400 °C/1 h → 498 °C/1 h) was implemented using a TEM foil to track the ⟨a⟩ and ⟨c⟩ loops evolution (Fig. 5c). Diffraction vector $\vec{g}$=0002 was employed to distinguish the ⟨a⟩ loops from the ⟨c⟩ loops. At 300 °C, both ⟨a⟩ and ⟨c⟩ loops experienced little changes in size and density, as shown in Fig. 5d. When the temperature increased to 400 °C, a significant reduction in the number density of ⟨a⟩ loops was noticed (see Fig. 5f and i), and subsequently the contrast of ⟨c⟩ loops become clearer, as shown in Fig. 5e. Numerous dislocation lines were observed at the same time, as displayed in Fig. 5f. With temperature continued to increase to 448 °C, the ⟨c⟩ loops start to interconnect and form kinked structures, as shown in Fig. S4, with dynamic evolution process captured by Movie S1. Subsequent annealing at 498 °C revealed the growth of ⟨a⟩ loops, and a large number of ⟨c⟩ loops with stacking fault contrast, as marked in Fig. 5 g. More and more ⟨c⟩ loops evolve from a flat configuration to a kinked morphology, as highlighted in Fig. 5h. The WBDF images in Fig. 6 confirmed that the kinked loops are all three-dimensional structures with a step connection at the middle point. In addition, several ⟨a⟩ dislocations are pinned at these steps (see Fig. 6), suggesting that the kinked ⟨c⟩ loops impede the gliding of ⟨a⟩ dislocations. With a further increase in the annealing temperature to 500 °C, the number density of kinked ⟨c⟩ dislocation loops steadily increases, while the number density of both ⟨a⟩ loops and flat ⟨c⟩ loops decreases, as illustrated in Fig. 5i.

4. Discussion

4.1. Formation of kinked ⟨c⟩ dislocation loop

The observations above suggest that the formation of three-dimensional kinked structures arises from the thermally activated evolution of planar ⟨c⟩ loops. Previous studies have established that ⟨c⟩ dislocation loops maintain structural stability and remain sessile on the basal plane within 300 °C-400 °C service temperature range [23–25]. Our in-situ annealing experiments corroborate this thermal stability threshold, showing no significant ⟨c⟩ loop configuration changes below 400 °C (Fig. 5e). Notably, progressive structural transformations emerge as temperature approach 500 °C, where initially planar ⟨c⟩ dislocation loops undergo three-dimensional morphological transitions, forming kinked geometries spanning multiple basal planes. Notably, in-situ TEM observations (Movie S1) reveal no evidence of pyramidal-plane glide mechanism for ⟨c⟩ loops. Instead, the ends of the two adjacent ⟨c⟩ loops gradually connected above 400 °C, ultimately generating the steps parallel to the $\{\bar{1}101\}$ plane.

To elucidate the atomistic mechanisms governing ⟨c⟩ loops interconnection, we further performed Molecular Dynamics (MD) simulations tracking ⟨c⟩ loop evolution at high temperatures. A straight

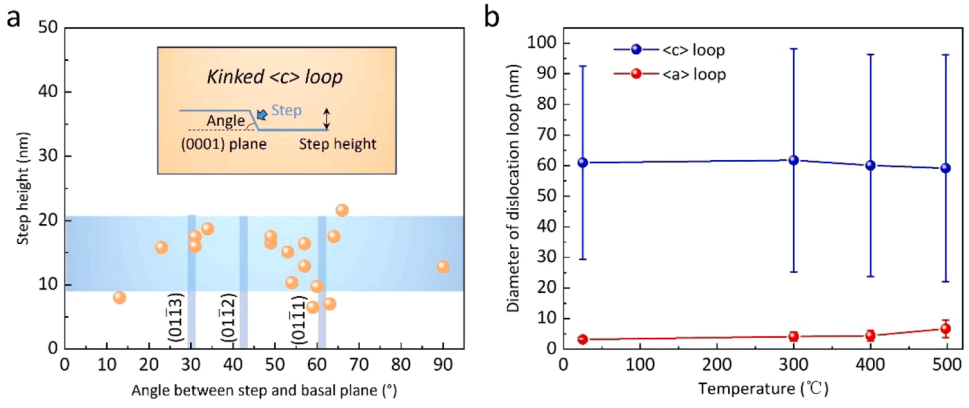

Fig. 4. Characteristics of ⟨c⟩ loops and ⟨a⟩ loops. (a) Statistics of the parameters of kinked ⟨c⟩ loops, such as the step height and the angle between the inclined step and the basal plane. (b) Variation of the size of ⟨a⟩ and flat ⟨c⟩ loops with annealing temperature.

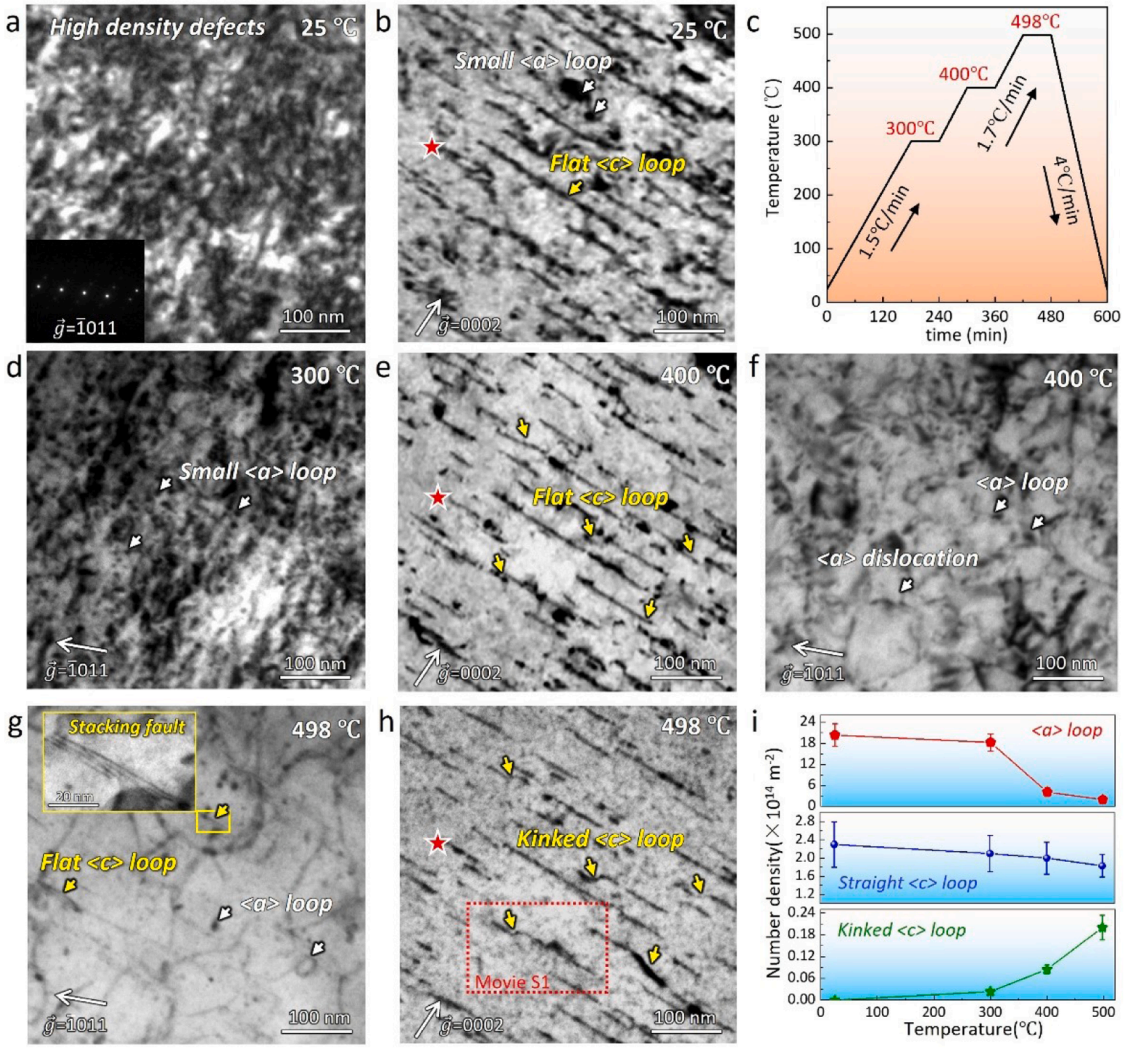

Fig. 5. Evolution of defects in Fe^{2+} irradiated pure Zr during in-situ annealing inside a TEM. (a) Irradiation induced ⟨a⟩ dislocation loops and (b) ⟨c⟩ dislocation loops. (c) In-situ annealing set up for pure Zr inside a TEM. The features of irradiation loops were characterized at the holding stages (60 mins) at each temperature, such as at (d) 300 °C, (f) 400 °C, and (g) 498 °C, respectively. (e) and (h) show the morphologies of ⟨c⟩ dislocation loops under $\vec{g}$=0002 diffraction condition at 400 °C and 498 °C. The red star is an anchor point to ensure the same observation area. (i) Variation of the number density of ⟨a⟩ loops, flat ⟨c⟩ loops and kinked ⟨c⟩ loops with increasing of the annealing temperature.

dislocation with Burgers vector of 1/6<$\bar{2}$203> was modeled to represent the endpoints of the ⟨c⟩ loops, as illustrated in Fig. 7a and f. Their spatial positional relationships align with the experimental geometries. After relaxation at 0 K, the 1/6<$\bar{2}$203> dislocation undergoes spontaneous dissociation: $\frac{1}{6}[\bar{2}203] = \frac{1}{6}[\bar{1}102] + SF_{\{\bar{1}101\}} + \frac{1}{6}[\bar{1}101]$, which leads to a 1/6[$\bar{1}$102] partial dislocation lying on the {$\bar{1}$101} plane, the residual 1/6[$\bar{1}$101] dislocation, as well as a stacking fault on the pyramidal (Pry.) I plane (Figs. 7b and S5a). Such dislocation dissociation has been widely reported and plays a critical role in the formation of stacking fault pyramids in Zr [34,35]. Fig. 7(b–e) and Movie S2 depict the evolution of two 1/6<$\bar{2}$203> straight dislocations at 1200 K. Owing to the elastic interaction between them, the 1/6 [$\bar{1}$102] partial dislocations with opposite Burgers vectors slip on the pyramidal plane, meet each other, and finally annihilate. This process leads to the formation of a stacking fault on the pyramidal plane. At 0.01 ns, a step parallel to the ($\bar{1}$101) plane is established (Fig. 7c). After that, the angle between the step and the basal plane gradually increases from 61° to 129°, culminating in the formation of a step parallel to the (1$\bar{1}$01) plane (Fig. 7d). Through this mechanism, the two flat ⟨c⟩ loops eventually form a zig-zag shape, as shown in Fig. 7f. Interestingly, pre-annealed endpoints of the two flat ⟨c⟩ loops exhibit partial spatial overlap (Fig. 7a and f). However, this phenomenon dissipates following the formation of the step (Fig. 7e), exhibiting excellent consistency with TEM observations (Fig. 7 g and h). Structural analysis identifies the step as a stable stacking fault along the <$\bar{1}$102> direction on the pyramidal plane {$\bar{1}$101} with a normalized displacement of approximately 1/6, as indicated by the corresponding stable stacking fault (see the stacking fault energy profile in Fig. S6). This multistep reconfiguration pathway, governed by partial dislocation glide energetics and stacking fault metastability, provides a universal framework for predicting annealing-induced defect evolution in irradiated HCP metals.

4.2. *Interaction force between adjacent ⟨c⟩ loops*

Regarding the formation mechanism of the kinked ⟨c⟩ loop, an essential question emerges: at experimentally relevant scales, can the mutual interaction between adjacent loops generate sufficient driving force to induce coordinated glide of partial dislocations? To address this, we first calculated the stress field surrounding one ⟨c⟩ loop and then systematically evaluated the interaction force between two nano-scale ⟨c⟩ loops.

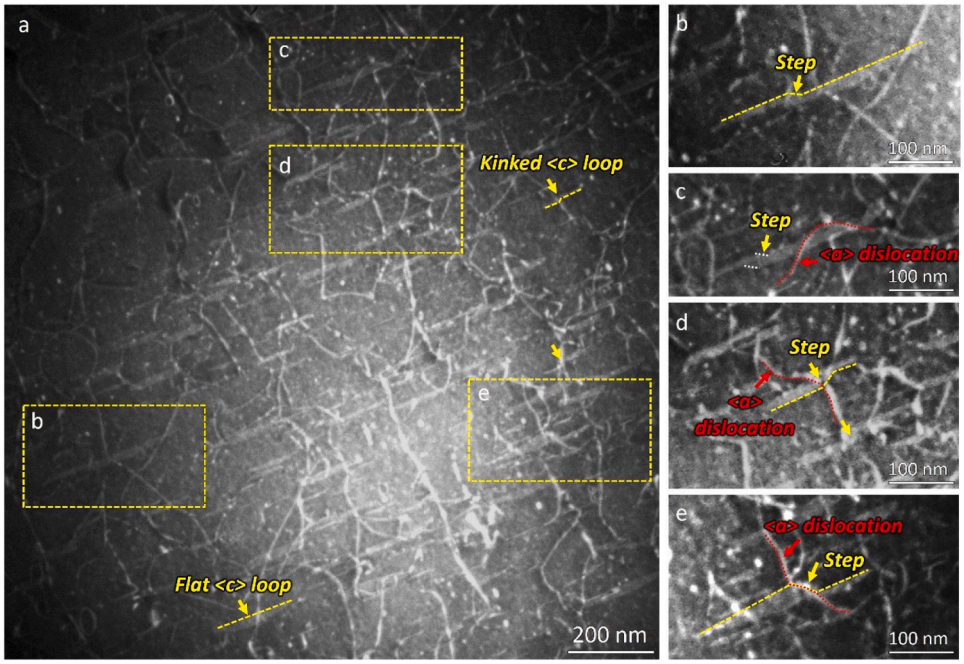

Fig. 6. Dark-field images of kinked ⟨c⟩ loops and their interaction with ⟨a⟩ loops in post-irradiation annealed Zr. (a) Weak-beam dark-field low-magnification TEM image of a kinked ⟨c⟩ dislocation loop after annealing under $\vec{g}=01\bar{1}0$ diffraction vector. (b-e) show the enlarged TEM image of three-dimensional ⟨c⟩ loops obstructing ⟨a⟩ loops. The red arrows indicate the pinned ⟨a⟩ dislocation lines at the steps.

The stress field surrounding the dislocation loop was determined by solving the Peach-Koehler equation for the self-stresses of any curved closed dislocation loop [44]:

$$\sigma_{\alpha\beta} = -\frac{G}{8\pi}\oint_C b_m \in_{im\alpha} \frac{\partial}{\partial x_i'} \nabla'^2 R dx_\beta' - \frac{G}{8\pi}\oint_C b_m \in_{im\beta} \frac{\partial}{\partial x_i'} \nabla'^2 R dx_\alpha' - \frac{G}{4\pi(1-\nu)}\oint_C b_m \in_{imk} \left(\frac{\partial^3 R}{\partial x_i' \partial x_\alpha' \partial x_\beta'} - \delta_{\alpha\beta} \frac{\partial}{\partial x_i'} \nabla'^2 R \right) dx_k' \quad (1)$$

where b_i is the ith component of the Burgers vector, $\in$ is the permutation symbol, G is the shear modulus and ν is Poisson's ratio. The results of the stress field surrounding a vacancy loop with the Burgers vector of $1/6 < 20\bar{2}3 >$ and a diameter of 6.7 nm determined by solving Eq. (1) are shown in Fig. 8. The results determined via molecular statics (MS) simulation are also shown for comparison (see Fig. 8b and c). In the MS simulation, a model of 29.0 nm × 30.1 nm × 29.3 nm was constructed, where a dislocation loop with the Burgers vector $b = 1/6 < 20\bar{2}3 >$ and a diameter of 6.7 nm was inserted. This structure was then relaxed by the conjugate gradient algorithm employing the LAMMPS code [32] and the EAM potentials developed by Mendelev and Ackland [33], and the stress components of each atom divided by Voronoi volume [45] were determined. It is seen that the stress fields surrounding the dislocation loop determined by these two methods agree well with each other.

Taking into account the stress field generated by loop$_1$, the interaction force $\boldsymbol{F}_{loop}(d)$ exerted by loop$_1$ on the bowing partial dislocation at Point A in loop$_2$ can be determined. Here, Point A is identified as the nearest point in loop$_2$ to loop$_1$, and d denotes the distance between the bowing partial dislocations (here denotes Point A to loop$_1$), as indicated in Figs. 7f and 8. According to the Peach-Koehler (PK) formula [45], the force per unit length $\boldsymbol{F}^{\mathrm{PK}}$ at an arbitrary point along a (possibly curved) dislocation line is

$$\boldsymbol{F}^{\mathrm{PK}} = (\boldsymbol{b}\cdot\boldsymbol{\sigma}) \times \boldsymbol{\zeta} \quad (2)$$

where $\boldsymbol{b}$ is the Burgers vector of the partial dislocation at Point A in loop$_2$, $\boldsymbol{\sigma}$ is the tensor of the stress field generated by loop$_1$, which is calculated according to Eq. (1), and $\boldsymbol{\zeta}$ is the local line tangent direction at Point A of loop$_2$. The cross product with $\boldsymbol{\zeta}$ ensures that the $\boldsymbol{F}^{\mathrm{PK}}$ is always perpendicular to the dislocation line itself. The glide component of the PK force acting on the dislocation in the Pry. I plane is

$$F^g = \boldsymbol{F}^{\mathrm{PK}} \cdot \boldsymbol{l}_g \quad (3)$$

where $\boldsymbol{l}_g$ is the glide direction vector of the partial dislocation on the Pry. I plane. The interaction force $\boldsymbol{F}_{loop}(d)$ was defined to be F^g as a function of d.

For experimentally observed 60 nm loops (TEM-measured), we calculate the interaction force $F_{loop}(d)$. Key parameter values required in Eqs. (1–3) are listed in Table 1. As shown in Fig. 8e, the interaction force at points A and A' as a function of d are positive, which means that the direction of the interaction force is the same as the vector of glide direction $\boldsymbol{l}_g$ and the two partial dislocations from two ⟨c⟩ loops will be in close proximity under the action of this force. We compare the interaction force $\boldsymbol{F}_{loop}(d)$ exerted by one loop on the bowing partial dislocation from the other loop against (i) the drag force $\boldsymbol{f}_{drag}$, which arises from the frictional stress of the partial dislocation and the requirement to create a stacking fault, and (ii) the line tension force $\boldsymbol{f}_{lt}(d)$ associated with dislocation curvature. Here, $\boldsymbol{f}_{drag}$ per unit length of the partial dislocation was estimated as $\boldsymbol{\tau}_{CRSS}\boldsymbol{b}$, where $\boldsymbol{\tau}_{CRSS}$ is the critical resolved shear stress of the partial dislocation slipping on the pyramidal plane along the growth direction of stacking fault.

As $d \to 0$, $\boldsymbol{F}_{loop}(d)$ increases steadily, whereas $\boldsymbol{f}_{drag}$ remains nearly constant. Meanwhile, $\boldsymbol{f}_{lt}(\boldsymbol{d})$ increases initially but then likely decreases, providing an activation energy for kinking rather than a significant thermodynamic driving force when d is comparable to or smaller than the loop size; in such cases, the overall dislocation line length before bowing out and after kink formation does not change substantially. Consequently, if $\boldsymbol{F}_{loop}(d)$ exceeds the drag force $\boldsymbol{f}_{drag}$ right after the partial dislocations bow out, the partials can progress toward the other partial, while necessary to overcome an activation barrier. Our estimates at 0 K show that $\boldsymbol{F}_{loop}(d) > \boldsymbol{f}_{drag}$ when the initial loop separation d satisfies d<10 nm or d<21 nm, depending on the initial positions of the loops (see Fig. 8e). This critical separation d is comparable to the average distance of 17 nm between loops in the experiment based on the

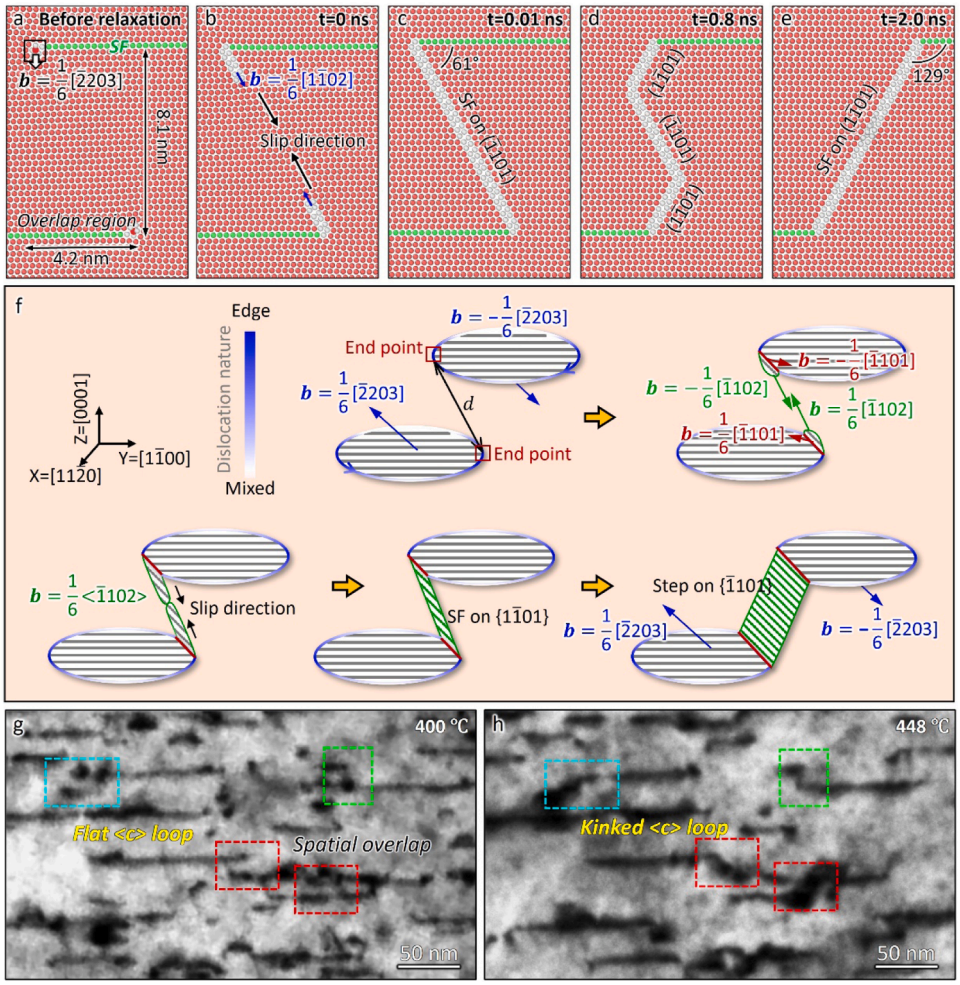

Fig. 7. Formation process of three-dimensional kinked ⟨c⟩ loop. (a-e) The interaction of two adjacent dislocation segments of ⟨c⟩ loop, leading to the formation of kinked ⟨c⟩ loop, derived from MD simulations. Atoms are color-coded based on the structure types analyzed via the Common Neighbor Analysis (CNA) and Dislocation Extraction Algorithm (DXA). (f) The evolution process of the kinked ⟨c⟩ loop. In fact, the Burgers vectors of the two ⟨c⟩ loops are identical. In order for the two dislocation lines at the endpoint to be congruent, the direction of the dislocation loops must be one clockwise and one counterclockwise, so that the Burgers vectors are labelled as opposite. (g) High magnification TEM images of flat ⟨c⟩ loops at 400 °C. After annealing at 448 °C, these flat ⟨c⟩ loops evolve into kinked ⟨c⟩ loops (h).

TEM images (see Fig. 4), suggesting that the partial dislocations from each loop could be capable of gliding toward each other owing to the interaction between two loops, with this phenomenon being more probable at higher temperatures. Complementary MD simulations at 1200 K demonstrate that spontaneous energy reduction during the transition from two planar ⟨c⟩ loops to kinked configurations (Fig. S7a). Strikingly, adjacent loops coalesce into larger defect structures through step-mediated interactions (see Fig. S7b), revealing a novel coarsening pathway for ⟨c⟩ dislocation loops.

A few hydrides were also observed in the irradiated samples, and they completely dissolved when the temperature increased to 400 °C during in-situ annealing within the TEM. Hydrogen may influence defect dynamics at ambient temperatures through vacancy trapping [6]. Thus, the influence of hydrogen on the evolution of ⟨c⟩ loops was also examined using the BMD19.2 EAM potential for the Zr-H system [46], coupled with hybrid MD/Grand Canonical Monte Carlo (GCMC) simulations [47]. This potential well-reproduces the interactions of H with Zr. For example, the binding energy of interstitial H and the trapping energy of H in vacancy were estimated as E_{bind}=−0.435 eV and $E_{vac,\ trap}$=−0.173 eV, which agree well with the *ab-initio* determined values of E_{bind}=−0.459 eV and $E_{vac,\ trap}$=−0.189 eV [46]. Fig. S8 shows that the hydrogen atoms are distributed homogeneously above 700 K, which minimizes impact on the three-dimensional kinking process during annealing.

4.3. Kinked-basal ⟨c⟩ loops for hardening

Both neutron-irradiated Zircaloys [17–20,28] and ion-irradiated pure Zr in this study exhibited anomalous hardening upon annealing above 400 °C. While solute redistribution and precipitate formation may contribute to hardening in alloy systems [28], these mechanisms are explicitly excluded in our high-purity Zr model material. In-situ annealing experiments reveal a temperature-dependent microstructural evolution. At 400 °C, numerous ⟨a⟩ dislocation loops undergo significant annihilation and coalescence (Fig. 5), correlating with the measured hardness reduction (Fig. 2). Upon reaching 500 °C, only sparse <*a*> loops and dislocation lines left. Notably, we observe a structural transformation where two-dimensional ⟨c⟩ dislocation loops evolve into three-dimensional kinked configurations through pyramidal-plane step formation, effectively immobilizing the defects [48].

The hardening contributed by these sensile kinked loops could be estimated by the dispersed barrier hardening (DBH) model [49]: $\Delta\sigma_{loop} = \alpha\mu b\sqrt{Nd}$, where α is typically referred to as a barrier strength coefficient, and here takes on the value of 0.3 for ⟨c⟩ loops [49], the shear modulus μ is 33 GPa, Burgers vector b of the faulted ⟨c⟩ loop is 2.94

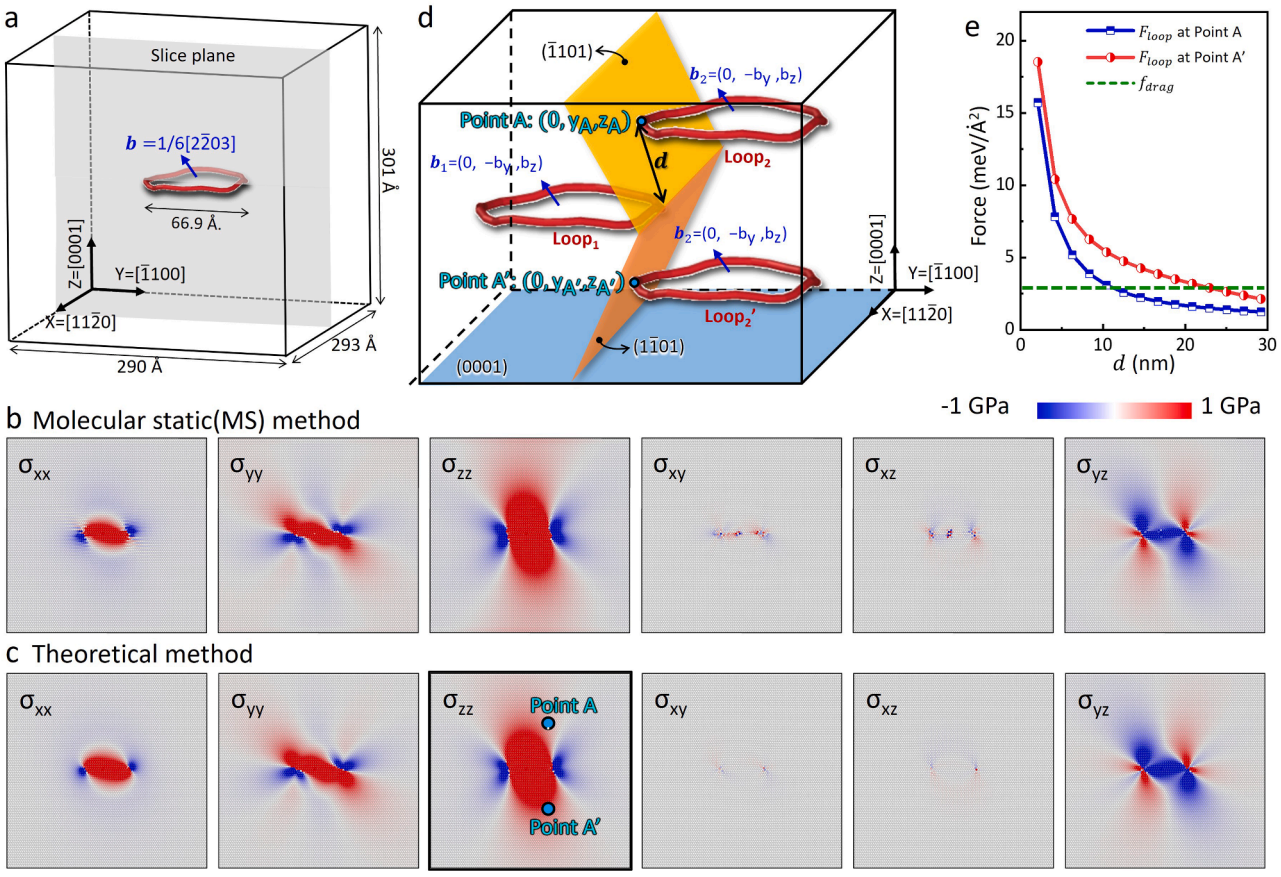

Fig. 8. Interaction force between two ⟨c⟩ loops. (a) The stress field model of one ⟨c⟩ loop. The components of the stress field surrounding the ⟨c⟩ loop on the (11$\bar{2}$0) slice, determined by (b) MS calculation and (c) theoretical method of Eq. (1). (d) The schematic diagram to determine the interaction force worked on point A of $loop_2$ and Point A' of $loop_2$' induced by the stress field of $loop_1$. There are two different spatial positions for $loop_2$ (marked $loop_2$ and $loop_2$' respectively) relative to $loop_1$. Owing to the symmetry of the stress field of ⟨c⟩ loop in Fig. S10c, the stress tensor at point A and point A' are different. (e) The interaction force $\boldsymbol{F_{loop}}(d)$ exerted by $loop_1$ on the bowing partial dislocation at Point A in $loop_2$ owing to the stress field generated by $loop_1$. The green dashed line shows the $\boldsymbol{f_{drag}}$ per unit partial dislocation length.

Table 1
Value of the parameters in Eqs. (1–3) used to determine the interaction force $\boldsymbol{F_{loop}}(d)$ in experimental scales. See Fig. 8 for the schematic diagrams of $Loop_2$ and $Loop_2$'.

Parameters in Eqs. (1–3)	$Loop_2$	$Loop_2$'
Burgers vector of partial dislocation $\boldsymbol{b} = 1/6 < \bar{1}102 >$ (Å)	$\boldsymbol{b}_1 = \boldsymbol{b}_2 = [0, -0.9293, +1.7163]$	
Local line tangent direction $\boldsymbol{\zeta}$	Point A and Point A': $\boldsymbol{\zeta} = [1,0,0]$	
Vector of glide direction $\boldsymbol{l_g}$	Glide direction on **Pry. I** plane of point A: $\boldsymbol{l_g} = [0,0.4792, -0.8777]$	Glide direction on **Pry. I** plane of point A': $\boldsymbol{l_g} = [0,0.4792, +0.8777]$

nm, the number density of kinked ⟨c⟩ loops is about N=2.5 × 10^{20} m^{-3} in Kr^{2+} irradiated Zr (Fig. S2), the average diameter of dislocation loops is d=100 nm. Thus, the increase in critical resolved shear stress by kinked loops alone is 145 MPa. Considiering the hardness and strength obey the three-time relationship [50], the increment of the hardness is approximately 435 MPa, which is in agreement with the hardening measured by the nanoindentation measurements. This confirms three-dimensional kinked ⟨c⟩ loops as the dominant source of post-irradiation annealing hardening.

Atomistic simulations were also conducted to elucidate the underlying strengthening mechanism. A model containing two ⟨c⟩ loops with the Burgers vector $\boldsymbol{b} = 1/6 < 20\bar{2}3 >$ was generated using the Babel package [51]. This was achieved by introducing a platelet of vacancies into the HCP Zr matrix, resulting in an ABABCBCB stacking sequences along the [0001] direction [36]. The model was then simulated at 1400 K in an NPT ensemble until step formation was observed. Subsequently, a 1/3⟨11$\bar{2}$0⟩ screw dislocation was introduced on various prismatic planes. Dislocation motion was driven by applying a constant velocity of 0.1 Å/ps parallel to the Burgers vector in the upper region, while the lower region remained fixed. This enables screw dislocation slip on the {1$\bar{1}$00} plane at 5 K. The peak shear stress along [11$\bar{2}$0] direction corresponds to the moment when the screw dislocation interacts with the loops.

When a screw ⟨a⟩ dislocation on the prismatic plane (01$\bar{1}$0) and (10$\bar{1}$0) interact with a kinked ⟨c⟩ loop (Fig. 9a–c), the stepped geometry induces repeated stress concentration during cutting events. Compared to planar loops, kinked configurations generate 50 % higher shear resistance (Fig. 9b and c). When the ⟨a⟩ dislocation cuts through the kinked loops, they are more likely to become pinned at this step and are dragged out after passing the loops, resulting in a dramatic hardening (see Movies S3-S6). This simulation is consistent with the experimental observation that several ⟨a⟩ dislocations are pinned at the steps of the kinked ⟨c⟩ loops, as marked in Fig. 9(d–f). The strengthening effect observed in the presence of three-dimensional kinked ⟨c⟩ dislocation loops is comparable to that of helium bubbles strengthening [52], as both act as a stronger barrier for the movement of the mobile ⟨a⟩ dislocations, leading to an increase in hardness or strength.

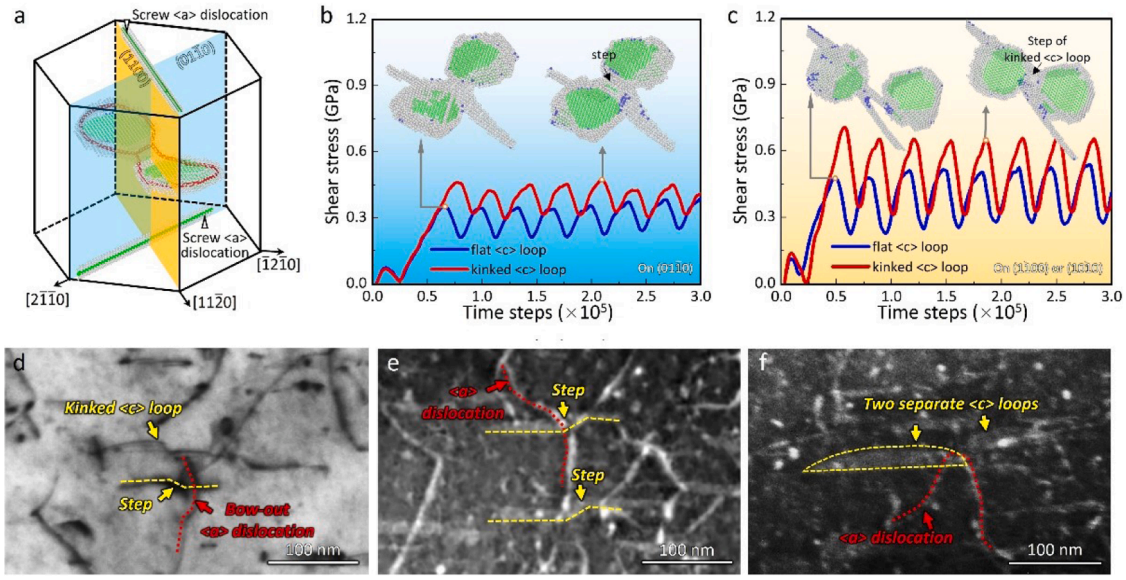

Fig. 9. Interaction of ⟨a⟩ dislocation with three-dimensional kinked ⟨c⟩ loop for hardening. (a) Atomistic model of a screw ⟨a⟩ dislocation on (01$\bar{1}$0) and (1$\bar{1}$00) cutting through a kinked ⟨c⟩ loop. (b) Variation of shear stress for a screw ⟨a⟩ dislocation on (01$\bar{1}$0) cutting through a flat ⟨c⟩ loop and a kinked ⟨c⟩ loop, respectively. (c) Variation of shear stress for a screw ⟨a⟩ dislocation on (1$\bar{1}$00) or (10$\bar{1}$0) cutting through a flat ⟨c⟩ loop and a kinked ⟨c⟩ loop, respectively. (d) TEM image showing a ⟨a⟩ dislocation obstructed by a kinked ⟨c⟩ loop. (e) TEM image of a ⟨a⟩ dislocations stopped at the step of a kinked ⟨c⟩ loop. (f) TEM image showing a ⟨a⟩ dislocation interacting with a single ⟨c⟩ loop.

5. Conclusions

In summary, our experimental observations and atomistic simulations reveal that a multi-stage defect evolution pathway in irradiated Zr: Initially basal-plane-aligned two-dimensional ⟨c⟩ loops evolve via thermally activated structural transformation into three-dimensional kinked configurations during 400 °C-500 °C annealing. This process initiates through partial dislocation dissociation from planar ⟨c⟩ loops, followed by pyramidal-plane slip and stacking fault reconstruction that enables geometric reconfiguration. The resultant three-dimensional kinked ⟨c⟩ loops could effectively impede the easy glide of ⟨a⟩ dislocations, thereby inducing anomalous annealing hardening in irradiated Zr. These findings fundamentally advance our understanding of post-irradiation defect dynamics in hexagonal close-packed metals. The identified mechanism provides critical insights into the long-term performance prediction of nuclear reactor cladding materials.

CRediT authorship contribution statement

Si-Mian Liu: Writing – review & editing, Writing – original draft, Methodology, Investigation, Funding acquisition. **Shi-Hao Zhang:** Writing – original draft, Visualization, Methodology, Investigation. **Hiroaki Abe:** Writing – review & editing, Methodology. **Shigenobu Ogata:** Writing – review & editing, Supervision, Funding acquisition. **Wei-Zhong Han:** Writing – review & editing, Writing – original draft, Supervision, Funding acquisition, Conceptualization.

Declaration of competing interests

The authors declare that they have no known competing financial interests or personal relationships that could have appeared to influence the work reported in this paper

Acknowledgments

S.M.L. gratefully thanks Dr. Huilong Yang at the University of Tokyo (currently Shanghai Jiaotong University) for the help in Fe^{2+} irradiation and high-temperature in situ TEM tests. S.M.L. and W.Z.H. thank Drs. Gaosheng Yan and Wenshan Yu at Xi'an Jiaotong University (XJTU) for the assistance in high-temperature nanoindentation tests. S.M.L. acknowledges the supports from the National Natural Science Foundation of China (Grant No. 52301019) and the China Postdoctoral Science Foundation (BX20220245 and 2024M752573). W.Z.H. acknowledges the supports by the Continuous Basic Scientific Research Project (BJ020261223286). S.H.Z. was funded by the JSPS KAKENHI Grant No. 25K17509. S.O. acknowledges the support by the Ministry of Education, Culture, Sport, Science and Technology of Japan (Grant Nos. JPMXP1122684766, JPMXP1020230325, and JPMXP1020230327), and the support by JSPS KAKENHI (grant nos JP23H00161 and JP23K20037). Part of the calculations were performed on the large-scale computer systems at the Cybermedia Center, The University of Osaka, the Large-scale parallel computing server at the Center for Computational Materials Science, Institute for Materials Research, Tohoku University, Research Center for Computational Science, Okazaki, Japan (Project: 24-IMS-C503), and supercomputer Fugaku provided by the RIKEN Center for Computational Science (Project IDs: hp250229 and hp250227).

Supplementary materials

Supplementary material associated with this article can be found, in the online version, at doi:10.1016/j.actamat.2025.121366.

References

[1] B.C. Masters, Dislocation loops in irradiated iron, Nature 200 (1963) 254.
[2] C. Cawthorne, E.J. Fulton, Voids in irradiated stainless steel, Nature 216 (1967) 576.
[3] P.T. Heald, M.V. Speight, Point-defect behavior in irradiated materials, Acta Metall. 23 (1975) 1389–1399.
[4] W. Xu, Y. Zhang, G. Cheng, W. Jian, P.C. Millett, C.C. Koch, S.N. Mathaudhu, Y. Zhu, In-situ atomic-scale observation of irradiation-induced void formation, Nat. Commun. 4 (2013) 2288.
[5] X.F. Kong, N. Gao, I.J. Beyerlein, B.N. Yao, R.F. Zhang, Interface facilitated transformation of voids directly into stacking fault tetrahedra, Acta Mater. 188 (2020) 623–634.
[6] S.M. Liu, I.J. Beyerlein, W.Z. Han, Two-dimensional vacancy platelets as precursors for basal dislocation loops in hexagonal zirconium, Nat. Commun. 11 (2020) 5766.

[7] F. Long, L. Balogh, D.W. Brown, P. Mosbrucker, T. Skippon, C.D. Judge, M. R. Daymond, Effect of neutron irradiation on the deformation mechanisms operating during tensile testing of Zr-2.5Nb, Acta Mater. 102 (2016) 352–363.
[8] B.V. Cockeram, R.W. Smith, K.J. Leonard, T.S. Byun, L.L. Snead, Development of microstructure and irradiation hardening of zircaloy during low dose neutron irradiation at nominally 358°C, J. Nucl. Mater. 418 (2011) 46–61.
[9] R.Y. Zheng, W.R. Jian, I.J. Beyerlein, W.Z. Han, Atomic-scale hidden point-defect complexes induce ultrahigh irradiation hardening in tungsten, Nano Lett. 21 (2021) 5798–5804.
[10] M.D. McMurtrey, G.S. Was, B. Cui, I. Robertson, L. Smith, D. Farkas, Strain localization at dislocation channel-grain boundary intersections in irradiated stainless steel, Int. J. Plast. 56 (2014) 219–231.
[11] S.H. Li, N. Gao, W.Z. Han, In-situ study of initiation and extension of nano-thick defect-free channels in irradiated nickel, J. Mater. Sci. Tech. 58 (2020) 114–119.
[12] K. Ehrlich, Irradiation creep and interrelation with swelling in austenitic stainless-steels, J. Nucl. Mater. 100 (1981) 149–166.
[13] G.S. Jawaharram, C.M. Barr, A.M. Monterrosa, K. Hattar, R.S. Averback, S. J. Dillon, Irradiation induced creep in nanocrystalline high entropy alloys, Acta Mater. 182 (2020) 68–76.
[14] R.B. Adamson, C.E. Coleman, M. Griffiths, Irradiation creep and growth of zirconium alloys: a critical review, J. Nucl. Mater. 521 (2019) 167–244.
[15] A. Kuramoto, T. Toyama, Y. Nagai, K. Inoue, Y. Nozawa, M. Hasegawa, M. Valo, Microstructural changes in a Russian-type reactor weld material after neutron irradiation, post-irradiation annealing and re-irradiation studied by atom probe tomography and positron annihilation spectroscopy, Acta Mater. 61 (2013) 5236–5246.
[16] Y. Higashiguchi, Y. Higashiguchi, Effect of hydrogen on the mechanical properties at high temperature of fast-neutron irradiated Ti alloys, J. Nucl. Mater. 103&104 (1981) 925–930.
[17] K. Veevers, W.B. Rotsey, K.U. Snowden, The effect of neutron irradiation and cold work on the strain-aging behavior of Zircaloy 2. Applications-Related Phenomena in Zirconium and Its Alloys, ASTM International, West Conshohocken, PA, 1969. Ed. Committee B-10, 100 Barr Harbor Drive, PO Box C700, 19428–2959.
[18] K.U. Snowden, K. Veevers, Radiation hardening in Zircaloy 2, Radia. Eff. 20 (1973) 169–174.
[19] T. Onchi, H. Kayano, Y. Higashiguchi, The inhomogeneous deformation behavior of neutron irradiated Zircaloy-2, J. Nucl. Mater. 88 (1980) 226–235.
[20] T. Torimaru, T. Yasuda, M. Nakatsuka, Changes in mechanical properties of irradiated Zircaloy-2 fuel cladding due to short term annealing, J. Nucl. Mater. 238 (1996) 169–174.
[21] Y. Idrees, Z. Yao, M.A. Kirk, M.R. Daymond, In situ study of defect accumulation in zirconium under heavy ion irradiation, J. Nucl. Mater. 433 (2013) 95–107.
[22] M. Topping, T. Ungár, C.P. Race, A. Harte, A. Garner, F. Baxter, S. Dumbill, P. Frankel, M. Preuss, Investigating the thermal stability of irradiation-induced damage in a zirconium alloy with novel in situ techniques, Acta Mater. 145 (2018) 255–263.
[23] A. Jostsons, R.G. Blake, J.G. Napier, P.M. Kelly, K. Farrell, Faulted loops in neutron-irradiated zirconium, J. Nucl. Mater. 68 (1977) 267–276.
[24] M. Griffiths, R.W. Gilbert, V. Fidleris, R.P. Tucker, R.B. Adamson, Neutron damage in zirconium alloys irradiated at 644 to 710K, J. Nucl. Mater. 150 (1987) 159–168.
[25] R.A. Holt, R.W. Gilbert, <c>component dislocations in annealed zircaloy irradiated at about 570 K, J. Nucl. Mater. 137 (1986) 185–189.
[26] M. Griffiths, R.A. Holt, A. Rogerson, Microstructural aspects of accelerated deformation of Zircaloy nuclear reactor components during service, J. Nucl. Mater. 225 (1995) 245–258.
[27] A. Jostsons, K. Farrell, Structural damage and its annealing response in neutron irradiated magnesium, Radia. Eff. 15 (1972) 217–225.
[28] B.V. Cockeram, K.J. Leonard, T.S. Byun, L.L. Snead, J.L. Hollenbeck, The recovery of irradiation damage for Zircaloy-2 and Zircaloy-4 following low dose neutron irradiation at nominally 358°C, J. Nucl. Mater. 461 (2015) 244–264.
[29] K. Murakami, T. Iwai, H. Abe, N. Sekimura, Improvement of the high fluence irradiation facility at the university of Tokyo, Nucl. Inst. Method. Phys. Res. B 381 (2016) 67–71.
[30] R.E. Stoller, M.B. Toloczko, G.S. Was, A.G. Certain, S. Dwaraknath, F.A. Garner, On the use of SRIM for computing radiation damage exposure, Nucl. Instrum. Methods Phys. Res. Sect. B 310 (2013) 75–80.
[31] C. Yan, R. Wang, X. Dai, Y. Wang, X. Wang, G. Bai, Y. Zhang, Investigation of hardening behavior in Xe ion-irradiated Zr-1Nb, J. Nucl. Mater. 473 (2016) 256–263.
[32] S. Plimpton, Fast parallel algorithms for short-range molecular dynamics, J. Comput. Phys. 117 (1995) 1–19.
[33] M.I. Mendelev, G.J. Ackland, Development of an interatomic potential for the simulation of phase transformations in zirconium, Philos. Mag. Lett. 87 (2007) 349–359.
[34] Y. Liu, C. Xu, X. Tian, W. Jiang, Q. Wang, H. Fan, Formation of stacking fault pyramid in zirconium, Comput. Mater. Sci. 212 (2022) 111591.
[35] B. Christiaen, C. Domain, L. Thuinet, A. Ambard, A. Legris, A new scenario for <c>vacancy loop formation in zirconium based on atomic-scale modeling, Acta Mater. 179 (2019) 93–106.
[36] C. Dai, C. Varvenne, P. Saidi, Z. Yao, M.R. Daymond, L.K. Béland, Stability of vacancy and interstitial dislocation loops in α-zirconium: atomistic calculations and continuum modelling, J. Nucl. Mater. 554 (2021) 153059.
[37] C. Varvenne, O. Mackain, E. Clouet, Vacancy clustering in zirconium: an atomic-scale study, Acta Mater. 78 (2014) 65–77.
[38] G. Henkelman, B. Uberuaga, H. Jónsson, A climbing image nudged elastic band method for finding saddle points and minimum energy paths, J. Chem. Phys. 113 (2000) 9901–9904.
[39] D. Faken, H. Jónsson, Systematic analysis of local atomic structure combined with 3D computer graphics, Comp. Mater. Sci. 2 (1994) 279–286.
[40] A. Stukowski, K. Albe, Extracting dislocations and non-dislocation crystal defects from atomistic simulation data, Model. Simul. Mater. Sc. 18 (2010) 085001.
[41] A. Stukowski, Visualization and analysis of atomistic simulation data with OVITO–the Open Visualization Tool, Model. Simul. Mater. Sc. 18 (2009) 015012.
[42] Y. Bu, Z. Li, J. Liu, H. Wang, D. Raabe, W. Yang, Nonbasal slip systems enable a strong and ductile hexagonal-close-packed high-entropy phase, Phys. Rev. Lett. 122 (2019) 075502.
[43] K. Srivastava, S.I. Rao, J.A. El-Awady, Unveiling the role of super-jogs and dislocation induced atomic-shuffling on controlling plasticity in magnesium, Acta Mater. 161 (2018) 182–193.
[44] J.P. Hirth, J. Lothe, Theory of Dislocations, Krieger Publishing Company, 1982.
[45] C. Rycroft, VORO++: a three-dimensional Voronoi cell library in C++, (2009).
[46] E. Wimmer, M. Christensen, W. Wolf, W.H. Howland, B. Kammenzind, R.W. Smith, Hydrogen in zirconium: atomistic simulations of diffusion and interaction with defects using a new embedded atom method potential, J. Nucl. Mater. 532 (2020) 152055.
[47] D. Frenkel, B. Smit, Understanding Molecular Simulation: From Algorithms to Applications, 2nd ed, 2002.
[48] D. Rodney, G. Martin, Y. Brechet, Irradiation hardening by interstitial loops: atomistic study and micromechanical model, Mater. Sci. Eng. A 309 (2001) 198–202.
[49] Ö. Koç, R. Thomas, X.Z. Liang, Z. Hegedüs, U. Lienert, R.W. Harrison, M. Preuss, T. Ungár, P. Frankel, A spatially resolved analysis of dislocation loop and nanohardness evolution in proton irradiated Zircaloys, Acta Mater. 269 (2024) 119799.
[50] P. Zhang, S.X. Li, Z.F. Zhang, General relationship between strength and hardness, Mater. Sci. Eng. A 529 (2011) 62–73.
[51] E. Clouet, Babel package version 10.7, 2022.URL http://emmanuel.clouet.free.fr/Programs/Babel/index.html.
[52] M.S. Ding, J.P. Du, L. Wan, S. Ogata, L. Tian, E. Ma, W.Z. Han, J. Li, Z.W. Shan, Radiation-induced helium nanobubbles enhance ductility in submicron-sized single-crystalline copper, Nano Lett. 16 (2016) 4118–4124.